



CHORUS

This is the accepted manuscript made available via CHORUS. The article has been published as:

Ultrafast resonant soft x-ray diffraction dynamics of the charge density wave in TbTe_3

R. G. Moore, W. S. Lee, P. S. Kirchman, Y. D. Chuang, A. F. Kemper, M. Trigo, L. Patthey, D. H. Lu, O. Krupin, M. Yi, D. A. Reis, D. Doering, P. Denes, W. F. Schlotter, J. J. Turner, G. Hays, P. Hering, T. Benson, J.-H. Chu, T. P. Devereaux, I. R. Fisher, Z. Hussain, and Z.-X. Shen

Phys. Rev. B **93**, 024304 — Published 25 January 2016

DOI: [10.1103/PhysRevB.93.024304](https://doi.org/10.1103/PhysRevB.93.024304)

Ultrafast resonant soft x-ray diffraction dynamics of the charge density wave in TbTe_3

R. G. Moore^{1,*}, W. S. Lee^{1,*}, P. S. Kirchman¹, Y. D. Chuang², A. F. Kemper^{1,3}, M. Trigo^{1,4}, L. Patthey^{1,5}, D. H. Lu⁶, O. Krupin^{7,8}, M. Yi¹, D. A. Reis^{1,4}, D. Doering², P. Denes², W. F. Schlotter⁸, J. J. Turner⁸, G. Hays⁸, P. Hering⁸, T. Benson⁸, J. -H. Chu⁹, T. P. Devereaux¹, I. R. Fisher⁹, Z. Hussain², and Z. -X. Shen^{1,*}

¹*Stanford Institute for Materials and Energy Sciences,*

SLAC National Accelerator Laboratory, Menlo Park, CA 94025, USA

²*Advanced Light Source, Lawrence Berkeley National Laboratory, Berkeley, CA 94720, USA*

³*Lawrence Berkeley National Laboratory, Berkeley, CA 94720, USA*

⁴*Stanford PULSE Institute for Ultrafast Energy Science,*

SLAC National Accelerator Laboratory, Menlo Park, CA 94025, USA

⁵*Swiss Light Source, Paul Scherrer Institut, CH-5232 Villigen-PSI, Switzerland*

⁶*Stanford Synchrotron Radiation Lightsource,*

SLAC National Accelerator Laboratory, Menlo Park, CA 94025, USA

⁷*European XFEL, Hamburg, Germany*

⁸*Linac Coherent Light Source, SLAC National*

Accelerator Laboratory, Menlo Park, CA 94025, USA and

⁹*Geballe Laboratory for Advanced Materials and Department of Applied Physics,*

Stanford University Stanford, CA 94305, USA

Abstract

Understanding the emergence of collective behavior in correlated electron systems remains at the forefront of modern condensed matter physics. Disentangling the degrees of freedom responsible for collective behavior can lead to insights into the microscopic origins of emergent properties and phase transitions. Utilizing optical pump, resonant soft x-ray diffraction probe we are able to track, in real time, the dynamics of the charge density wave (CDW) in TbTe_3 , a model system that violates traditional views of a Fermi surface (FS) nested CDW. We observe coherent oscillations corresponding to the CDW amplitude mode at 2.4 THz and a coherent optical phonon mode at ~ 1.7 THz. We show how such observations reveal the anisotropic energy optimization between in-plane Te charge density modulations and the 3D lattice coupling.

PACS numbers: 71.45.Lr, 78.47.J-, 61.05.cp, 63.20.kd

I. INTRODUCTION

Electronic instabilities are at the core of phenomena such as density waves, colossal magnetoresistance and superconductivity¹⁻³. The key to understanding such exotic many body states is disentangling the contributions from the coupled degrees of freedom. Density waves, both of charge and spin, have been studied for decades and a wealth of information has been gained¹. While containing interesting properties deserving of attention in their own right, as model systems the insights gained from understanding the density wave phenomena have implications far beyond these material systems themselves. The stripe phase in high-Tc cuprate superconductors, for example, is analogous to a unidirectional CDW and TbTe₃ under pressure reveals the interplay between superconductivity, magnetic and charge order^{4,5}. However, there are still open questions that need to be resolved for a complete description of the density wave phenomena. While one dimensional systems are well described by Peierls 2k_F instabilities¹, this understanding is absent in systems of higher dimensions. For example, there are several existing systems that exhibit prototypical behavior while traditional theory focusing on Fermi surface nesting fails to capture the underlying physics^{6,7}. The family of the rare-earth tritellurides (RTe₃) is a well known example of a seemingly prototypical FS nested CDW system but the direction of the CDW is 45° from that predicted by electronic susceptibility calculations at the FS⁷⁻¹².

The RTe₃ family crystallizes in the weakly orthorhombic NdTe₃ structure, space group *Cmcm*, consisting of two planar Te nets sandwiched between buckled RTe slabs as shown in Fig. 1a. The electronic structure near the Fermi energy is dominated by the in-plane Te *p_x* and *p_z* orbitals, noting that the *b*-axis is the long axis in this structure^{7,11-14}. X-ray and STM analysis of TbTe₃ reveal an incommensurate lattice modulation characterized by a single wave vector along the *c*-axis ($\mathbf{q}_{CDW} \approx 0.71 \times 2\pi/c$) at $T = 50$ K^{13,15,16}. Angle resolved photoemission spectroscopy (ARPES) shows a gapped portion of the FS along the CDW direction^{11,17}. The temperature dependence of the order parameter follows familiar BCS trends in both x-ray¹³ and photoemission data¹² with a smooth filling in of the energy gap and correlation lengths orders of magnitude longer than the lattice constants. Heavier rare-earth family members even exhibit a second CDW that once again gaps the FS despite an already reconstructed electronic structure from the first CDW¹². Time resolved ARPES (tr-ARPES) shows the gap is intrinsically linked to the CDW amplitude mode, a collective

excitation corresponding to a modulation of the CDW amplitude from its equilibrium value, which is at the core of CDW physics¹⁷⁻²².

With extensive experimental results illustrating intricate details of the CDW state, a theoretical model describing the underlying microscopic mechanisms still remains elusive. By modeling a square Te net, Yao *et al.*⁴ demonstrated that due to the underlying quasi-one dimensionality of the Te bands a unidirectional CDW is favored, but LDA calculations by Johannes *et al.*⁷ show the CDW wave vector to be rotated 45° from the direction predicted by the electronic susceptibility that focuses only on contributions from the FS. When the complete band structure is accounted for then the correct wave vector is predicted. However, there is no divergence or large response in the susceptibility as one would expect from a low dimensional material, only a small enhancement. Such discrepancies led the authors to conclude that the FS plays little role, if any, in the formation of the CDW state⁷.

A focusing effect due to electron-phonon interactions has been invoked to explain the more robust nature of the CDW in 2-dimensions^{4,23,24}. For example, it has been argued the next nearest neighbor hopping between Te atoms that lifts the band degeneracy at the FS p_x and p_z band crossings can create a focusing effect in the electron-phonon coupling favoring the crystalline axis of the unit cell and thus the observed CDW direction²⁴. Inelastic x-ray scattering has confirmed a momentum dependent electron-phonon coupling that favors the observed q_{CDW} ²⁵. Time resolved electron diffraction measurements also show an anisotropy between the a and c-axis which further demonstrates the importance of electron-phonon coupling even along the different in plane crystalline axis²⁶.

Here we report time resolved resonant soft x-ray diffraction experiments in TbTe₃ to directly examine the interplay between lattice and charge degrees of freedom in the formation of the CDW state. The diffraction peak resulting from the long range CDW order was monitored while optically exciting the material. Coherent oscillations were observed at 2.4 THz and 1.7 THz which can be assigned to the CDW amplitude mode and a lattice optical phonon, respectively, indicating the strongly coupled nature of the charge and lattice degrees of freedom in the CDW state. By considering the atomic motions of the optical phonon mode, shown to mix with the amplitude mode^{19,20,27}, and lattice strain induced by atomic motions along different FS nesting vectors we are able to show how anisotropic lattice strain energy favors CDW formation along the experimentally observed q_{CDW} .

II. EXPERIMENTAL DETAILS

Single crystals of TbTe_3 were grown by slow cooling a binary melt as described elsewhere^{13,28}. The CDW phase transition temperature for TbTe_3 is approximately 340K. The crystals were oriented along the [010] direction using Laue diffraction and cleaved prior to insertion into the vacuum chamber. The sample was then cooled to $\approx 50\text{K}$ for the measurements.

Time resolved soft x-ray resonant diffraction experiments were performed using the RSXS endstation at the SXR instrument of the Linac Coherent Light Source (LCLS)^{29,30}. The dynamics of the $(0, 4, q_{CDW})$ diffraction peak were measured while optically pumping at 3 mJ/cm^2 with a 50 fs 800 nm laser pulse generated utilizing a Ti:sapphire laser amplifier system as schematically shown in Fig. 1b. The LCLS was operated in the high charge (250 pC, 70 fs) mode at 60 Hz repetition rate and a diffraction image for every shot was recorded by a compact fast x-ray CCD (fCCD) camera with representative images shown in Fig. 2a³¹. X-ray absorption spectrum measurements of the Tb M_5 edge were used to calibrate the x-ray energy. The photon energy of the x-ray probe pulse was set to the Tb M_5 edge corresponding to the $3d - 4f$ transition in Tb. It should be noted that the diffraction peak due to a CDW modulation in the Te planes is observed while resonantly exciting an electronic transition in the Tb atoms of neighboring planes as the Tb atoms feel the electrostatic modulation by the Te density wave³².

Each LCLS shot was normalized by the incident photon flux (I_0) as measured by the photocurrent generated from an in-line aluminum foil. A mechanical delay stage with encoded position readout was used to adjust the delay time between the laser pump - x-ray probe pulses. A phase cavity was utilized to correct for the inherent LCLS timing jitter resulting in a $\approx 300 \text{ fs}$ timing resolution³³. A fCCD dark frame was generated by averaging ~ 200 images taken with the LCLS x-ray shutters closed and subtracted from every fCCD image. Diffraction peak intensity was measured by integrating a 150×150 pixel wide region centered around the peak.

Due to monochromatization of the x-ray beam, any energy jitter from the LCLS results in a x-ray intensity jitter on the sample. The fCCD camera has inherent thermal and electronic noise and the weak x-ray pulses, with small I_0 , will amplify these noise fluctuations during normalization. A critical component in analyzing the data is to create an I_0 threshold

to eliminate the weaker x-ray intensity outliers that can degrade the signal-to-noise ratio and distort the data. Figures 3a and 3b shows the implications of the I_0 thresholding. To determine the appropriate I_0 threshold, the standard error for all LCLS shots prior to time zero was calculated for different threshold levels as shown in Fig. 3a. Since the peak intensity is expected to be static prior to time zero, minimizing the standard error will maximize the signal-to-noise ratio. Setting the threshold too high will eliminate too many shots and statistical fluctuations will degrade the resulting data. It should be noted that eliminating $\approx 20 - 30\%$ of the weaker x-ray pulses is a good rule of thumb for the unseeded LCLS shots when measuring with the fCCD. The data above the threshold are normalized and then binned according to their jitter corrected delay time. All shots are averaged within each time bin as shown in Fig. 2a. Different time bin widths were considered and yielded similar results as shown below, thus a 60 fs time bin was typically used for the analysis.

III. RESULTS

A. Diffraction Peak Dynamics

Upon inspection of Fig. 2a a slow recovery time, on the order of ~ 1 ns when modeled with a single exponential (see Appendix), is immediately apparent while the CDW diffraction peak is still observed after pumping. The observed diffraction peak after the arrival of the pump pulse, which we define as time zero, could be a finite volume artifact due to the larger ~ 60 nm probe depth compared to the estimated ~ 35 nm pump depth. It should be emphasized that the recovery time observed in Fig. 2 is orders of magnitude larger than the few ps recovery observed in other time resolved measurements with similar pump fluence^{18,19,26}. While the larger probe depth could skew the observed recovery times slightly, it is unlikely to account for the orders of magnitude difference. The lack of significant width change in the diffraction peak shown in Fig. 4b suggests the difference between our observed recovery time and previous results is likely due to phase fluctuations as observed in other charge ordered materials²⁹. These incoherent CDWs can depress the diffraction intensity but cannot be detected by previous dynamics experiments that measure only the gap and thus the CDW amplitude. However, since the resonant x-ray process involves transitions between Tb's occupied and unoccupied $4f$ multiplets, the pump could also alter the occupation level

of these multiplets, resulting in a suppression of the diffraction intensity and overestimation of the CDW recovery time³².

Previous x-ray diffraction experiments have observed a slight change in q_{CDW} ($\Delta q_{CDW} \sim 1.4\%$) with temperature near the CDW transition¹³. To measure whether q_{CDW} changes in the pump-probe process, data were taken at detector angles on each side of the rocking curve maximum as shown in Fig. 2b. Any changes in q_{CDW} would result in a shift of the rocking curve resulting in an anisotropy in the spectra from each side of the rocking curve maximum. The anisotropy in the spectra on each side of the rocking curve is shown in Fig. 2b and is considered negligible. In addition, as the CDW peak is not resolution limited by the fCCD pixels, a shift of q_{CDW} would also cause a change of the peak position on the fCCD detector. Two dimensional Lorentz functions were fit to the averaged fCCD image for each delay time as shown in Fig. 4a and Fig. 4b. The shift in the diffraction peak observed on the fCCD image translates into a maximum 0.4% change in q_{CDW} and the width of the diffraction peak shows negligible change after pumping. As emphasized in the Fig. 2b inset, there is a shift of the coherent oscillation peaks in the spectra between the rocking curve maximum and the two sides which is likely due to the dispersion of the coherent modes, reminiscent of the dispersion of coherent phonons³⁴. Unfortunately, the reduction in the signal-to-noise ratio off the rocking curve maximum precludes any quantitative analysis in the current data. Future experiments with improved statistics or different techniques would likely make such a dispersion measurement possible³⁵.

While q_{CDW} and the width of the diffraction peak show little change after pumping, oscillation in both of these fit parameters are observed for delay times < 2 ps as shown in Fig. 4a and 4b. These oscillations are well above the noise level and suggest a time dependent and/or frequency dependent q_{CDW} and coherence length of the CDW order. Future experiments with improved statistics will quantify such trends. In this report, we will focus on analyzing the coherent oscillations observed in the CDW diffraction peak intensity.

B. Data Fitting and Fourier Analysis

For the first few picoseconds after time zero intensity oscillations are observed. No oscillations are observed in the time dynamics of the (0, 4, 0) lattice Bragg peak shown in Fig. 2a

inset suggesting the oscillations are coherent modes intrinsically linked to the underlying CDW state. To better evaluate the coherent modes, a smooth background is subtracted from averaged data as detailed in the Appendix. The pronounced decrease of the diffraction intensity after time zero and the sloping background at later delay times precludes Fourier transforming the transient diffraction intensity directly and requires subtraction of phenomenological background. The goal is to obtain an oscillatory trace without step-like features or slow variations and thus enable a clear identification of the coherent modes in the Fourier spectrum.

In the Appendix we show that by performing various Fourier transformations the coherent modes are independent of details of the phenomenological background, the size of the time bins, and the window being Fourier transformed, which underlines the robustness of our observations. The experimental results used for our physical interpretation are summarized in Fig. 5 and Fig. 6.

While the residual intensity oscillations are near the noise level they are still resolved, even in the raw data of Fig. 2a, and represents the first coherent oscillations observed from a resonant soft x-ray experiment. The FT amplitudes within a 0 – 4 ps window show three peaks above the background. We assign the peak centered at ~ 2.4 THz to be the amplitude mode of the CDW in agreement with other experiments^{17,19,20,27}. Lattice modes with similar energy have been observed in other measurements but no coherent oscillations appear in the lattice Bragg peak as shown in Fig. 2a inset and one would expect the amplitude mode to be a dominant feature in the CDW diffraction peak dynamics^{19,20,25,27}. In addition, there are two large peaks in Fig. 6 near 1.2 THz and 1.7 THz. The distance between the peaks of the first two oscillation is ~ 0.66 ps ~ 1.5 THz as shown in Fig. 5 which is consistent with the dominant FT peaks in Fig. 6 but also suggests that these features could be one single mode distorted by the limited resolution and number of oscillations observed. To check the FT results, the residual data were fit with a three sinusoidal mode model as shown in Fig. 5. The model fit frequencies and amplitudes are consistent with those from the FT analysis as shown in Fig. 6.

C. Theoretical Mode Analysis

To understand the origins of the observed modes, Density Functional Theory (DFT) calculations were performed using the Quantum ESPRESSO³⁶ package (version 5.0) using ultrasoft pseudopotentials. We used the Perdew-Burke-Ernzerhof³⁷ formulation for the exchange-correlation functional within GGA. To obtain the energies of the phonon modes, we performed calculations of the dynamical matrix with a kinetic energy cutoff of 500 eV and a 13x3x13 momentum grid for the plane-wave basis. Energies were converged with respect to the number of k-points and both wavefunction energy cutoff and density energy cutoff converged to 30 meV. The dynamical matrix was subsequently diagonalized to obtain the eigenmodes of atomic displacements. Time resolved reflectivity and Raman data suggest the 1.7 THz mode is a lattice phonon mode that mixes with the CDW amplitude mode at $T \approx 250$ K^{19,20,27}. Thus we assume that the 1.7 THz mode is a normal state optical phonon mode and identify the atomic displacements, shown in Fig. 7, by noting the resulting frequencies of oscillation, and their trends as both the momentum grid and energy cutoff are increased. The 1.2 THz mode is harder to identify as there are several modes similar in energy as shown in Fig. 8. Due to the ambiguity in mode assignment and lack of observed mixing with the CDW amplitude mode the 1.2 THz mode is not a focus in this work.

To investigate the relative cost in strain between the two proposed directions of atomic motion in the CDW, i.e. along the 001 and 101 directions (as shown in orange and purple arrows, respectively, in Fig. 7), we performed single-point total energy calculations for a 2x2x1 (3D) supercell as a function of displacement distance. We created a $q = 0$ distortion of the unit cell along the indicated displacement pattern and displaced the involved atoms an equal amount. Since the CDW is incommensurate, it is difficult to create a supercell large enough to model atomic distortions modulated by the observed q -vector. This calculation assumes that all the atoms participating in the CDW are displaced the full amount; leading to an ordering vector in the calculation which is shorter than experimentally observed. As a result, the absolute scale of the displacement energy is overestimated compared to the CDW energy. Nevertheless, the comparison between the two directions is still valid. Our calculations show that the cost of atomic displacement along the 101 (purple) direction is higher than along the 001 (orange) direction as shown in Fig. 9. This suggests that the presence of the Tb ions causes a steric hindrance in the 101 direction and changing the

ordering vector to the experimentally observed one costs less in energy.

IV. DISCUSSION

The mode frequencies shown in Fig. 6 agree remarkably well with previous tr-ARPES^{17,22}, Raman²⁷ and reflectivity²⁰ experiments. Such agreement gives confidence in the FT analysis and mode assignment despite the limited number of oscillations and signal to noise limitations. Both Raman and reflectivity data observe the ~ 1.7 THz mode and show that it mixes with the amplitude mode at a temperature just below the CDW T_c and thus will be the focus of our discussion^{20,27}. The mode that best fits the experimental frequency is the optical mode shown in Fig. 7a. It is not surprising that all the atoms within the unit cell move in concert as part of the eigenmode. What is surprising is the level of interaction between the Te and Tb motions revealed in the phonon calculations graphically expressed as different arrow lengths for different Te atoms in Fig. 7a. While a layered system, the inter-layer coupling between the Te and neighboring Tb planes nevertheless creates site-dependent motions of Te atoms within the CDW plane. Figure 7b emphasize this anisotropy depicted as different arrow lengths for atoms within the same Te plane. To understand the implications of these site-dependent motions, we need to understand how atomic displacements connect to the nested Fermi surface shown in Fig. 7c and Fig. 9a. Assuming an in-plane longitudinal density wave, the total energy for Te displacements along the different nesting directions in Fig. 9a is calculated and shown in Fig. 9b. The inter-layer coupling resulting in the large anisotropy for the Te motions within the CDW plane translates into a large anisotropy in total energy for a strained lattice in the different nesting directions. The ideal nesting direction based on the shape of the FS (purple arrow in Fig. 9a) costs more in strain energy due to the buckled RTe slab. Such a large anisotropy in lattice coupling and strain energy implies a large anisotropy in the electron-phonon coupling. The CDW ground state is the result of an energy minimization and the energy reduction in the electronic structure must be balanced with the lattice strain energy incurred.

Previous works have demonstrated there exists an interplay between the 1.7 THz mode and the CDW amplitude mode^{20,27}. The simple fact that the 1.7 THz mode appears as a dominant feature in the time resolved dynamics of the CDW diffraction data suggests it has an important relation to the CDW amplitude mode and possibly the underlying CDW

mechanisms. The interplay and mixing between the 1.7 THz mode and the amplitude mode demonstrates the importance and directionality of coupling between lattice motions and the electronic instability imposed by the electronic structure. Such anisotropy in electron-phonon coupling and strain energy is not accounted for in traditional susceptibility calculations at the FS. Previous studies have observed anisotropic electron-phonon coupling in these materials²⁴⁻²⁶, but our results yield new insights in to the origins of the anisotropy and the delicate energy balance that creates the broken symmetry ground state.

It is common to find layered materials exhibiting emergent behavior with large unit cells encompassing many layers. The large 3D structures result in potentials that fold electronic bands back into reduced Brillouin zones, but the folding potentials are often weak resulting in electronic structures that are still highly 2D. While band folding creates an ideal FS nesting condition in TbTe₃, the buckled TbTe slab is viewed as a simple charge reservoir determining the Fermi level but having little implications on the dimensionality of the electronic structure¹¹. In contrast, the electronic structure may appear 2D but phonon modes still involve the entire 3D lattice. While the charge density modulations exist in the Te plane^{15,38} and the amplitude mode is connected to oscillations of the gapped in-plane p_x and p_z bands, the strain energy and electron-phonon coupling are significantly different between the c -axis and the 45° nesting directions.

V. CONCLUSIONS

We have measured the time resolved diffraction dynamics of lattice distortions resulting from the CDW order in TbTe₃. We observed coherent oscillations from the CDW amplitude mode at 2.4 THz and from a lattice optical phonon at 1.7 THz. Theoretical investigations resolve the atomic motions of the 1.7 THz phonon and show how the motions of atoms within the Te plane are dramatically affected by the neighboring Tb atoms. Calculations of the lattice strain energy shows that Te displacements along the direction that best nests the electronic FS cost more in energy than the displacements that nest the second best region of the FS. Our results emphasize the importance of lattice strain energy and anisotropy when determining the ground state of systems with coupled degrees of freedom.

ACKNOWLEDGMENTS

The authors thank D. Leuenberger for insightful discussions. This research was supported by the U.S. Department of Energy, Office of Science, Basic Energy Science, Materials Sciences and Engineering Division, SLAC National Accelerator Laboratory (SLAC), Stanford Institute for Materials and Energy Science (R.G.M., W.S.L., A.F.K., M.T, L.P., D.A.R., T.P.D., Z.X.S), SLAC Stanford Synchrotron Radiation Lightsource (D.H.L.) and under contract number DE-AC02-05CH11231 Lawrence Berkeley National Laboratory (LBNL) Advanced Light Source (Y.D.C., Z.H.), and LBNL Engineering Division (D.D., P.D.). P.S.K acknowledges support by the Alexander-von-Humboldt Foundation through a Feodor-Lynen scholarship. D.H.L acknowledges the support by the DOE award number DE-AC02-05CH11231. The SXR Instrument at LCLS is funded by a consortium whose membership includes LCLS, Stanford University - SIMES, LBNL, University of Hamburg through the BMBF priority program FSP 301, and the Center for Free Electron Laser Science (CFEL).

Appendix: Background Subtraction and Fourier Analysis

In the following we detail what steps were taken to ensure that the resulting Fourier spectrum is independent of the details of the model background, the size of the time bins the raw data is sorted into, and the length of the time window the Fourier transform is applied to.

We begin with a discussion of different phenomenological backgrounds. In all investigated models, the suppression of the diffraction intensity after arrival of the pump pulse is modeled by a step function that is calculated using a Gaussian error function with full-width-half-maximum w . The time delay when the intensity has dropped to half of its initial equilibrium value is given by t_0 and defines time-zero in our experiments. We investigated polynomial backgrounds up to 4th order N (Equation A.1) and single exponential recovery of the diffraction intensity with a time constant τ (Equation A.2). Here, a_i are free parameters of the fits.

$$BG_{\text{poly}}(t) = \left(\sum_{i=0}^N a_i (t - t_0)^i \right) \left(1 + \operatorname{erf} \left(\frac{2\sqrt{2}(t - t_0)}{w} \right) \right) / 2 \quad (\text{A.1})$$

$$BG_{\text{exp}}(t) = (a_0 + a_1 \exp(-(t - t_0)/\tau)) \left(1 + \operatorname{erf} \left(\frac{2\sqrt{2}(t - t_0)}{w} \right) \right) / 2 \quad (\text{A.2})$$

Figure 10 compares different models for background subtraction. All analysis was performed on the data set with a bin size of 60 fs. Due to the slow recovery of the signal on a nanosecond time scale even the crudest model, which subtracts only a constant background after time zero is able to extract the coherent oscillations. While increasing the polynomial order generates a smoother residual at later times it tends to perform suboptimal around the initial step. Figure 10c focuses on the behavior of the traces for background subtraction after the initial intensity decrease. Note that due to the slow recovery of the signal the 1st order polynomial effectively gives the same result as a single exponential recovery with the fitted time constant of $\tau = 1160(250)$ ps. While the limited amount of data yields a large error in the fit, it is clear that our observed recovery is significantly slower than observed in previous experiments^{18,19,26}.

Figure 11 depicts the resulting Fourier transforms of the residuals after background subtraction for 60 fs bins and a time window ranging from 0 to 8 ps, which corresponds to a nominal frequency resolution of 0.13 THz. This comparison evidences that details of the background subtraction do not influence the coherent modes we can identify in the Fourier spectrum. We thus chose a single exponential recovery, which allows to extract a recovery time constant.

In a next step we investigate the dependence of the Fourier transforms on the bin size, which directly changes the statistics of each data point, and the length of the time window being Fourier transformed, which relates to the nominal frequency resolution in the Fourier spectrum. The results are shown in Fig. 12. Again, the coherent modes can be clearly identified in all traces and do not depend on the choice of bin width and window size.

¹ G. Grüner, *Density waves in solids* (Addison-Wesley, Reading, MA, 1994).

² E. Dagotto, *Science* **309**, 257 (2005).

³ H. Y. Hwang, Y. Iwasa, M. Kawasaki, B. Keimer, N. Nagaosa, and Y. Tokura, *Nature Mater.* **11**, 103 (2012).

⁴ H. Yao, J. A. Robertson, E.-A. Kim, and S. A. Kivelson, *Phys. Rev. B* **74**, 245126 (2006).

- ⁵ J. J. Hamlin, D. A. Zocco, T. A. Sayles, M. B. Maple, J.-H. Chu, and I. R. Fisher, *Phys. Rev. Lett.* **102**, 177002 (2009).
- ⁶ K. Rossnagel, *J. Phys. Condens. Matter* **23**, 213001 (2011).
- ⁷ M. D. Johannes and I. I. Mazin, *Phys. Rev. B* **77**, 165135 (2008).
- ⁸ E. DiMasi, M. C. Aronson, J. F. Mansfeld, B. Foran, and S. Lee, *Phys. Rev. B* **52**, 14516 (1995).
- ⁹ G.-H. Gweon, J. D. Denlinger, J. A. Clack, J. W. Allen, C. G. Olson, E. DiMasi, M. C. Aronson, B. Foran, and S. Lee, *Phys. Rev. Lett.* **81**, 886 (1998).
- ¹⁰ V. Brouet, W. L. Yang, X. J. Zhou, Z. Hussain, N. Ru, K. Y. Shin, I. R. Fisher, and Z. X. Shen, *Phys. Rev. Lett.* **93**, 126405 (2004).
- ¹¹ V. Brouet, W. L. Yang, X. J. Zhou, Z. Hussain, R. G. Moore, R. He, D. H. Lu, Z. X. Shen, J. Laverock, S. B. Dugdale, et al., *Phys. Rev. B* **77**, 235104 (2008).
- ¹² R. G. Moore, V. Brouet, R. He, D. H. Lu, N. Ru, J.-H. Chu, I. R. Fisher, and Z.-X. Shen, *Phys. Rev. B* **81**, 073102 (2010).
- ¹³ N. Ru, C. L. Condrón, G. Y. Margulis, K. Y. Shin, J. Laverock, S. B. Dugdale, M. F. Toney, and I. R. Fisher, *Phys. Rev. B* **77**, 035114 (2008).
- ¹⁴ J. Laverock, S. B. Dugdale, Z. Major, M. A. Alam, N. Ru, I. R. Fisher, G. Santi, and E. Bruno, *Phys. Rev. B* **71**, 085114 (2005).
- ¹⁵ A. Fang, N. Ru, I. R. Fisher, and A. Kapitulnik, *Phys. Rev. Lett.* **99**, 046401 (2007).
- ¹⁶ A. Banerjee, Y. Feng, D. M. Silevitch, J. Wang, J. C. Lang, H.-H. Kuo, I. R. Fisher, and T. F. Rosenbaum, *Phys. Rev. B* **87**, 155131 (2013).
- ¹⁷ F. Schmitt, P. S. Kirchmann, U. Bovensiepen, R. G. Moore, L. Rettig, M. Krenz, J.-H. Chu, N. Ru, L. Perfetti, D. H. Lu, et al., *Science* **321**, 1649 (2008).
- ¹⁸ F. Schmitt, P. S. Kirchmann, U. Bovensiepen, R. G. Moore, J.-H. Chu, D. H. Lu, L. Rettig, M. Wolf, I. R. Fisher, and Z.-X. Shen, *New J. Phys.* **13**, 063022 (2011).
- ¹⁹ R. Yuzupov, T. Mertelj, V. V. Kabanov, S. Brazovskii, P. Kusar, J.-H. Chu, I. R. Fisher, and D. Mihailovic, *Nature Phys.* **6**, 681 (2010).
- ²⁰ R. V. Yuzupov, T. Mertelj, J.-H. Chu, I. R. Fisher, and D. Mihailovic, *Phys. Rev. Lett.* **101**, 246402 (2008).
- ²¹ L. Rettig, J.-H. Chu, I. R. Fisher, U. Bovensiepen, and M. Wolf, *Faraday Discuss.* **171**, 299 (2014).
- ²² D. Leuenberger, J. A. Sobota, S.-L. Yang, A. F. Kemper, P. Giraldo-Gallo, R. G. Moore, I. R.

- Fisher, P. S. Kirchmann, T. P. Devereaux, and Z.-X. Shen, *Phys. Rev. B* **91**, 201106(R) (2015).
- ²³ T. Kiss, T. Yokoya, A. Chainani, S. Shin, T. Hanaguri, M. Nohara, and H. Takagi, *Nature Phys.* **3**, 720 (2007).
- ²⁴ H.-M. Eiter, M. Lavagnini, R. Hackl, E. A. Nowadnick, A. F. Kemper, T. P. Devereaux, J.-H. Chu, J. G. Analytis, I. R. Fisher, and L. Degiorgi, *Proc. Nat. Acad. Sci.* **110**, 64 (2013).
- ²⁵ M. Maschek, S. Rosenkranz, R. Heid, A. H. Said, P. Giraldo-Gallo, I. R. Fisher, and F. Weber, *Phys. Rev. B* **91**, 235146 (2015).
- ²⁶ T.-R. T. Han, T. Zhensheng, S. D. Mahanti, C.-Y. Chang, K. Ruan, C. D. Malliakas, and M. G. Kanatzidis, *Phys. Rev. B* **86**, 075145 (2012).
- ²⁷ M. Lavagnini, H.-M. Eiter, L. Tassini, B. Muschler, R. Hackl, R. Monnier, J.-H. Chu, I. R. Fisher, and L. Degiorgi, *Phys. Rev. B* **81**, 081101(R) (2010).
- ²⁸ N. Ru and I. R. Fisher, *Phys. Rev. B* **73**, 033101 (2006).
- ²⁹ W. S. Lee, Y. D. Chuang, R. G. Moore, Y. Zhu, L. Patthey, M. Trigo, D. H. Lu, P. S. Kirchmann, O. Krupin, M. Yi, et al., *Nature Comms.* **3**, 838 (2012).
- ³⁰ W. F. Schlotter, J. J. Turner, M. Rowen, P. Heimann, M. Holmes, O. Krupin, M. Messerschmidt, S. Moeller, J. Krzywinski, R. Soufli, et al., *Rev. Sci. Instrum.* **83**, 043107 (2012).
- ³¹ D. Doering, Y. D. Chuang, N. Andresen, K. Chow, D. Contarato, C. Cummings, E. Domning, J. Joseph, J. S. Pepper, B. Smith, et al., *Rev. Sci. Instrum.* **82**, 073303 (2011).
- ³² W. S. Lee, A. P. Sorini, M. Yi, Y. D. Chuang, B. Moritz, W. L. Yang, J.-H. Chu, H. H. Kuo, A. G. Cruz Gonzalez, I. R. Fisher, et al., *Phys. Rev. B* **85**, 155142 (2012).
- ³³ J. M. Glowina, J. Cryan, J. Andreasson, A. Belkacem, N. Berrah, C. I. Blaga, C. Bostedt, J. Bozek, L. F. DiMauro, L. Fang, et al., *Optics Express* **18**, 17620 (2010).
- ³⁴ A. M. Lindenberg, I. Kang, S. L. Johnson, T. Missalla, P. A. Heimann, Z. Chang, J. Larsson, P. H. Bucksbaum, H. C. Kapteyn, H. A. Padmore, et al., *Phys. Rev. Lett.* **84**, 111 (2000).
- ³⁵ M. Trigo, M. Fuchs, J. Chen, M. P. Jiang, M. Cammarata, S. Fahy, D. M. Fritz, K. Gaffney, S. Ghimire, A. Higginbotham, et al., *Nature Phys.* **9**, 790 (2013).
- ³⁶ P. Giannozzi, S. Baroni, N. Bonini, M. Calandra, R. Car, C. Cavazzoni, D. Ceresoli, G. L. Chiarotti, M. Cococcioni, I. Dabo, et al., *J. Phys. Condens. Matter* **21**, 395502 (2009).
- ³⁷ J. P. Perdew, K. Burke, and M. Ernzerhov, *Phys. Rev. Lett.* **77**, 3865 (1996).
- ³⁸ H. J. Kim, C. D. Malliakas, A. T. Tomić, S. H. Tessmer, M. G. Kanatzidis, and S. J. L. Billinge, *Phys. Rev. Lett.* **96**, 226401 (2006).

FIG. 1. (a) Crystal Structure of TbTe_3 with unit cell outlined in blue. (b) Experimental geometry of the optical pump (red), resonant soft x-ray probe (blue) technique.

FIG. 2. (a) Experimental data normalized to incident photon flux showing the time dynamics of the $(0, 4, q_{CDW})$ diffraction peak and the $(0, 4, 0)$ Bragg peak (inset). Red dots are data from every LCLS shot while black line shows averaged data within 60 fs wide time bins. The inset fCCD images are from a single LCLS shot before and after time zero. (b) Normalized data for different diffraction angles depicted in the top right rocking curve inset. Lower left inset highlights dashed region of spectra showing shift in coherent oscillation peaks resulting from dispersion of coherent modes.

FIG. 3. (a) Standard error for all LCLS shots before time zero for a particular I_0 threshold. (b) Comparison of the standard deviation for all diffraction intensity measurements within a particular delay time bin with and without I_0 thresholding. The data without thresholding in (b) are shifted vertically upward for clarity.

FIG. 4. (a) Relative change in peak position from two dimensional Lorentzian fit. (b) Change in diffraction peak width from two dimensional Lorentzian fit. Error bars are based on pixel-by-pixel counting statistics and a weighted Lorentzian fit. It should be noted that q_c is along the crystalline c-axis, in the direction of q_{CDW} , while q_a is along the a-axis, orthogonal to q_{CDW} .

FIG. 5. Normalized data and background fit (top) and residual intensity after background subtraction with three mode sinusoidal fit (bottom).

FIG. 7. (a) Calculated atomic displacements of the 1.7 THz mode. Arrows lengths are proportional to displacement. The red dotted oval emphasize the interaction of Te motion constrained by the neighboring Tb layer. (b) Te motions within a single Te layer resulting from the out of plane interactions. Green square outlines 2D Te net and red square outlines 3D crystal unit cell. (c) Atomic motions for the total energy calculations in Fig. 9 for the different nesting directions.

FIG. 8. Potential candidates for the observed 1.2 THz mode. (a) Mode with calculated energy closest to the observed 1.2 THz. (b) Doubly degenerate mode (motions along either a or c-axis) with calculated energy of 1.1 THz.

FIG. 9. (a) Tight binding model of Fermi surface in first Brillouin zone. Solid red (blue) lines are the p_x (p_z) bands from 2D Te net and dashed lines are 2D Te bands folded back into the reduced Brillouin zone due to weak 3D potentials. Orange arrow shows CDW nesting vector realized in the material and purple arrow represents electronic susceptibility maximum from LDA calculations at the FS⁷. (b) Total energy difference calculated for Te displacements along orange and purple nesting direction in Fig. 7c. The results show displacements along c-axis cost less in energy.

FIG. 6. Fourier transform amplitude for a 0 – 4 ps time window of the residual intensity data. Vertical bars represent frequency and amplitude of three mode sinusoidal fit and reflectivity measurements from Ref.²⁰.

FIG. 10. (a) Background subtraction of a single exponential according to Equation. A.2. (b) 4th order polynomial background subtraction after Equation A.1. Background subtraction performed on the data set with 60 fs bins. Please note that the diffraction intensity is plotted on a logarithmic scale to enhance the visibility of the small oscillations. (c) Comparison of different models for background subtraction with focus on the low intensity region after the initial step.

FIG. 11. Fourier transforms of the residuals for different model backgrounds for 60 fs bins and a time window ranging from 0 to 8 ps, which corresponds to a nominal frequency resolution of 0.13 THz.

FIG. 12. Comparison of Fourier transforms for different bin sizes and increasing lengths of the time windows. The nominal frequency resolution in frequency space is indicated. (a) Bins with 18 fs width. (b) Bins with 60 fs width.

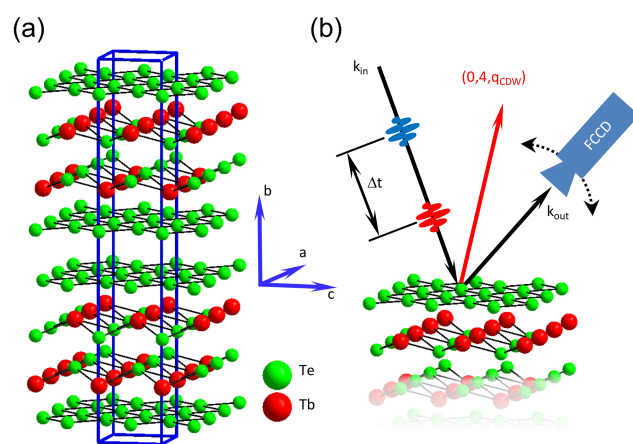


Figure 1

06Jan2016

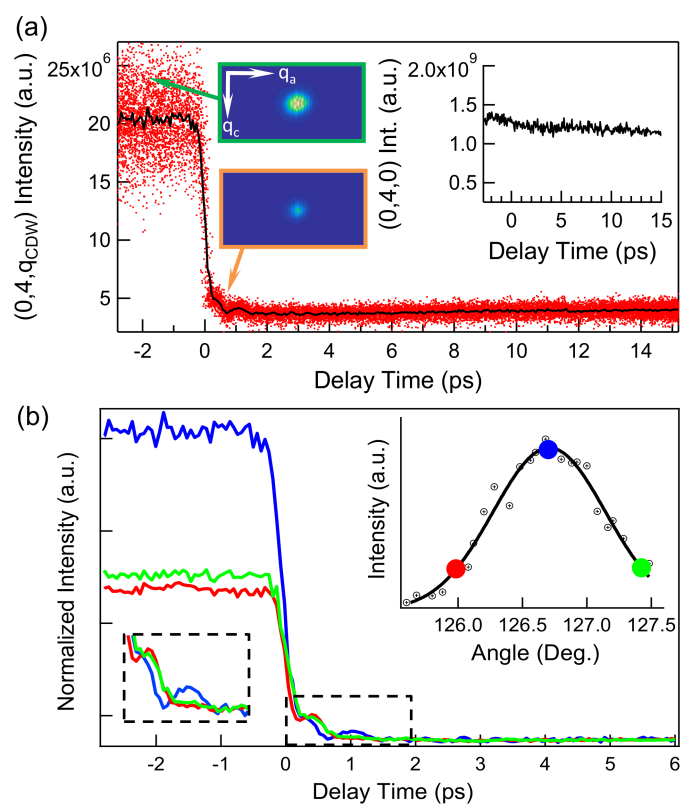


Figure 2

06Jan2016

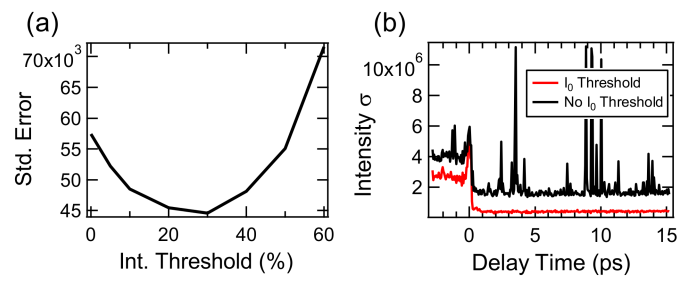


Figure 3

06Jan2016

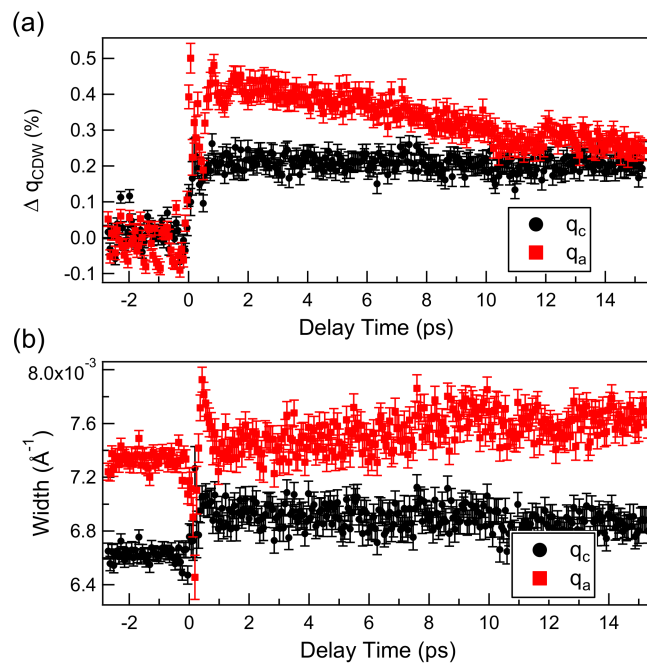


Figure 4

06Jan2016

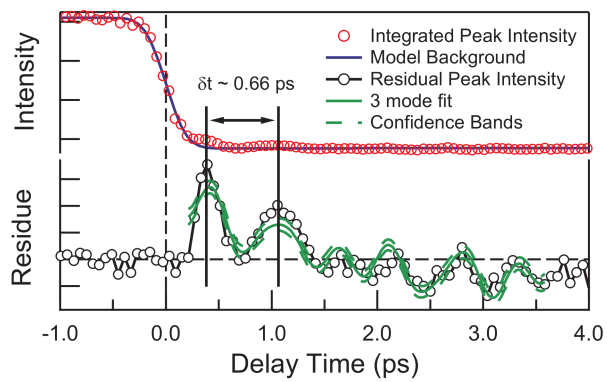


Figure 5

06Jan2016

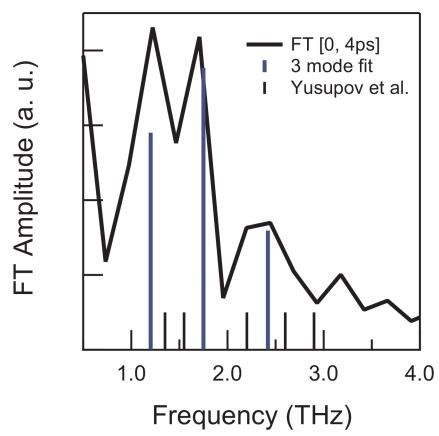


Figure 6

06Jan2016

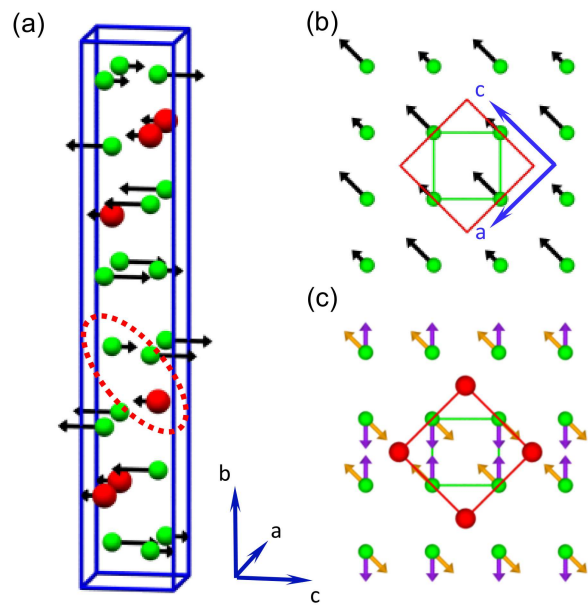


Figure 7

06Jan2016

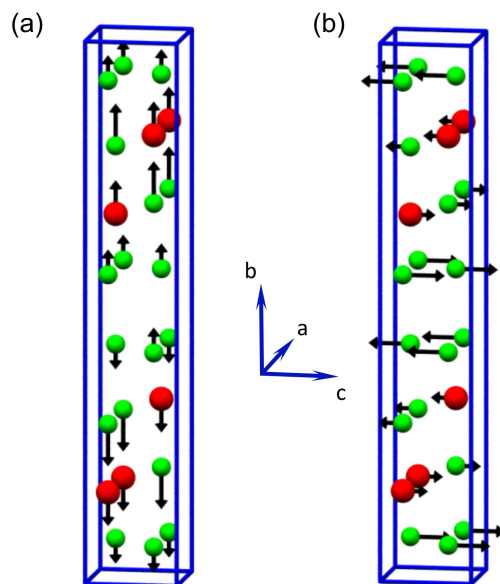


Figure 8

06Jan2016

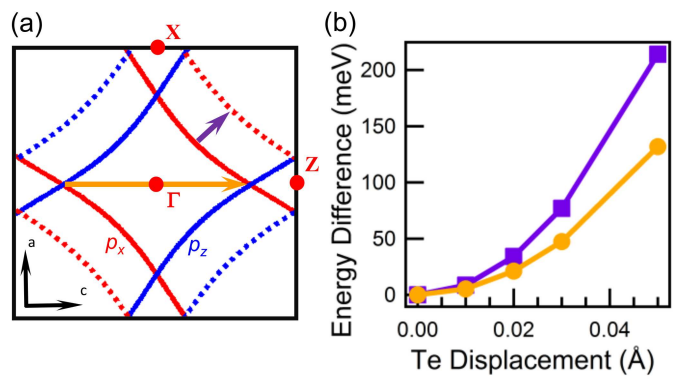


Figure 9

06Jan2016

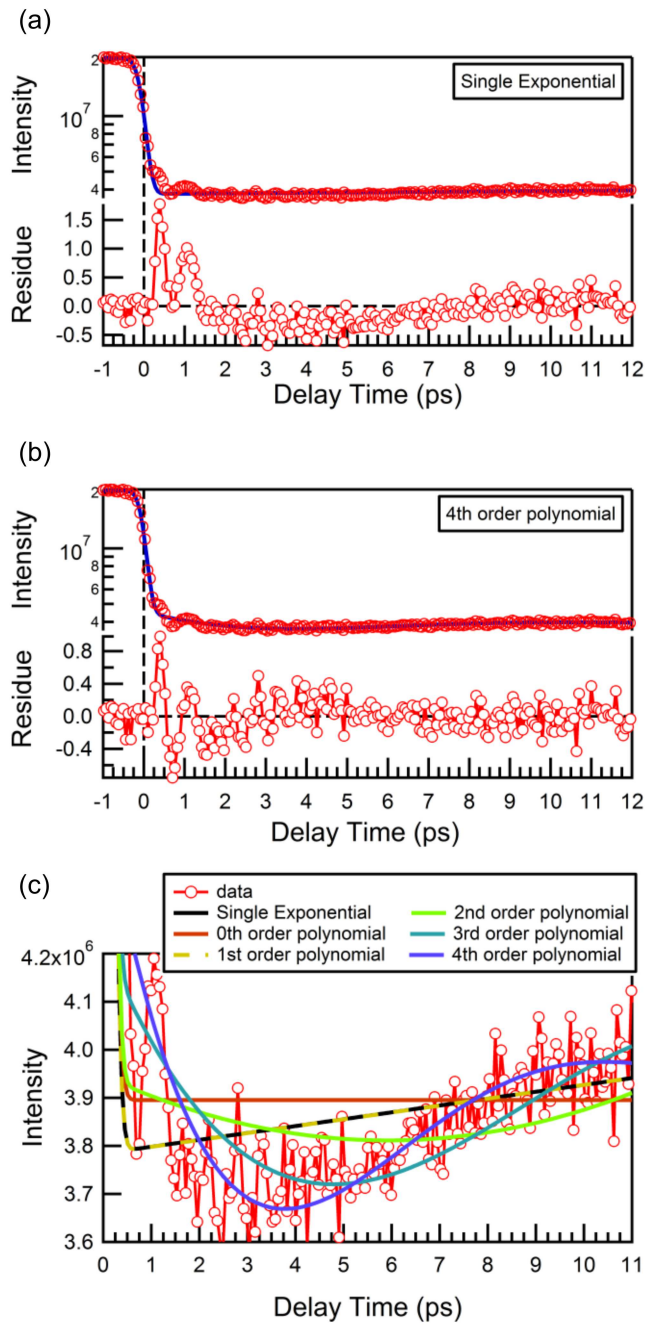


Figure 10

06Jan2016

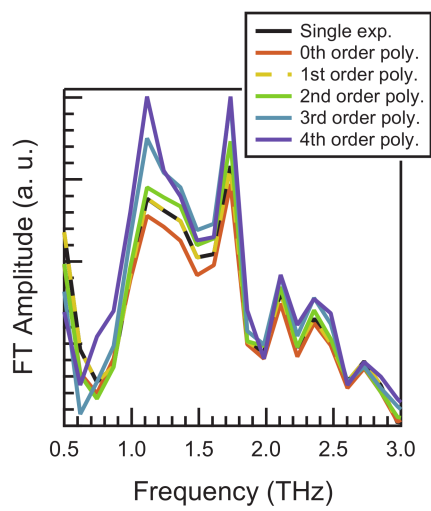


Figure 11

06Jan2016

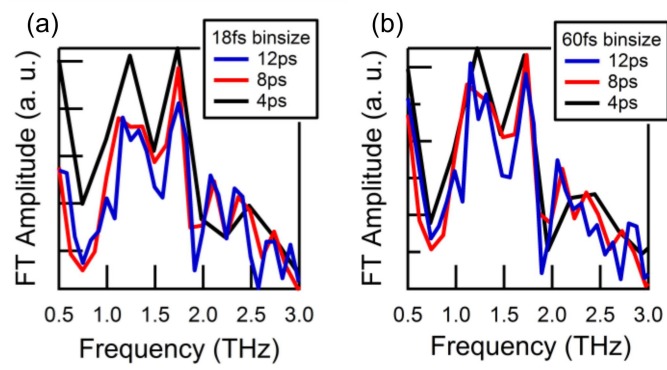


Figure 12

06Jan2016